

Dynamic Proximal Unrolling Network for Compressive Sensing Imaging

Yixiao Yang, Ran Tao, *Senior Member, IEEE*, Kaixuan Wei, Ying Fu, *Member, IEEE*

Abstract—Recovering an underlying image from under-sampled measurements, Compressive Sensing Imaging (CSI) is a challenging problem and has many practical applications. Recently, deep neural networks have been applied to this problem with promising results, owing to its implicitly learned prior to alleviate the ill-posedness of CSI. However, existing neural network approaches require separate models for each imaging parameter like sampling ratios, leading to training difficulties and overfitting to specific settings. In this paper, we present a dynamic proximal unrolling network (dubbed DPUNet), which can handle a variety of measurement matrices via one single model without retraining. Specifically, DPUNet can exploit both embedded physical model via gradient descent and imposing image prior with learned dynamic proximal mapping leading to joint reconstruction. A key component of DPUNet is a dynamic proximal mapping module, whose parameters can be dynamically adjusted at inference stage and make it adapt to any given imaging setting. Experimental results demonstrate that the proposed DPUNet can effectively handle multiple CSI modalities under varying sampling ratios and noise levels with only one model, and outperform the state-of-the-art approaches.

Index Terms—Dynamic Proximal Unrolling Network, Image Reconstruction, Compressive Sensing.

I. INTRODUCTION

Compressive Sensing Imaging (CSI) depicts a novel imaging paradigm for image acquisition and reconstruction that allows the recovery of a latent image from far fewer measurements than Nyquist sampling rate [1–4], and drives a range of practical applications, such as image or video compressive sensing [2, 5], compressive sensing magnetic resonance imaging (CS-MRI) [6, 7], single-pixel imaging [3, 8] and compressive phase retrieval (CPR) [9, 10].

Mathematically, given under-sampled measurements $y \in \mathbb{R}^M$ and compressive sensing model $\Phi(\cdot)$, the goal of CSI is to find a solution $\hat{x} \in \mathbb{R}^N$, such that $y \approx \Phi(\hat{x})$ and \hat{x} resides the class of images. Since the sampling ratio, defined as $\frac{M}{N}$, is typically much less than one, reconstructing a unique solution from limited measurements only is difficult or impossible without proper image priors.

To tackle the fundamental ill-posedness of CSI problems, traditional methods typically exploit the measurement model

This work was supported by the National Natural Science Foundation of China (62001023, U1833203), Beijing Natural Science Foundation (JQ20021), China Postdoctoral Science Foundation (2020M670163) (corresponding author: Ran Tao; e-mail: rantao@bit.edu.cn).

Y. Yang and R. Tao are with the School of Information and Electronics, Beijing Institute of Technology, Beijing 100081, China (e-mail: yixiayang@bit.edu.cn; rantao@bit.edu.cn).

K. Wei and Y. Fu are with the School of Computer Science and Technology, Beijing Institute of Technology, Beijing 100081, China (e-mail: kaixuan.wei@bit.edu.cn; fuying@bit.edu.cn).

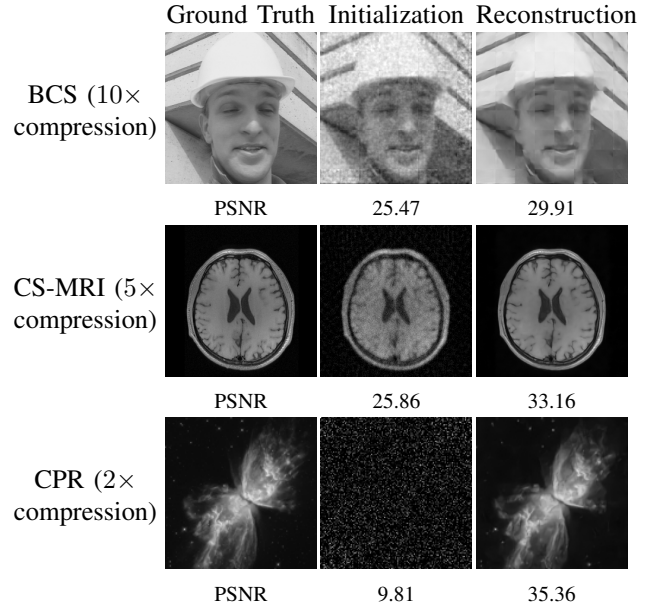


Fig. 1. Single trained model of our network is used to handle multiple CSI modalities with different sampling ratios: block-based compressive sensing (BCS) with $10\times$ compression, CS-MRI with $5\times$ compression, and CPR with $2\times$ compression. Note that even though these CSI problems are very different, the proposed network can handle multiple imaging modalities under various imaging conditions via only one trained model without retraining.

knowledge and intrinsic image properties [11–16], and solve a regularized optimization problem in an iterative scheme [17–22]. They are effective and flexible to handle a wide variety of measurements based on well-studied forward model and well-understood behavior, but limit in high computational complexity and challenges of tuning parameters.

In contrast to iterative-based methods, deep learning based CSI approaches [23–26], as an alternative, employ neural networks to directly learn mapping from measurements to latent quantities entirely based upon data. Once trained, the inference only requires a single forward of the network, without the need of time-consuming optimization and hyper-parameters selection. Nevertheless, pure deep learning approach cannot offer the flexibility of variational methods in adapting to different CSI modalities and even sampling ratios, largely due to learning a task-specific mapping. Traditionally one would require separate deep network for each imaging setting even if there is only a tiny change, which limits its practical applications.

Motivated by the observation that many iterative optimization algorithms can be truncated and unfolded into learnable deep neural networks, researchers have explored the hybrid

approach (*i.e.*, deep unrolling) that combines the best of both worlds in CSI [27–30]. Following the unrolling, regularizers or any other free hyper-parameters such as the step size or regularization parameters, can be learned via end-to-end training, rather than being hand-crafted, meanwhile the physical measurement model can be explicitly exploited. In this way, deep unrolling networks take the merits of interpretability and flexibility of optimization-based methods and fast inference of deep learning based approaches, while achieving promising reconstruction performance.

Despite these gains, the existing deep unrolling networks still suffer from severe performance degradation when operating on measurement matrix significantly different from training setting. An illustrative example on image compressive sensing is shown in Fig. 2, where the model trained on fixed sampling ratio (“fixed”) produces poor results when testing on unseen sampling ratios during training. While the performance can be improved when training on all sampling ratios jointly (“all”), there is still a large gap between such model and the task-specific model separately trained on each sampling ratio (“optimal”).

In fact, the ill-posedness of CSI problems and difficulties of learning to solve the corresponding inverse problem are very distinct under different imaging conditions. Furthermore, learned parameters of a specific unrolling network remain fixed after training, so the inference cannot adapt dynamically to other imaging parameter configurations. To address the aforementioned issue, in this paper, a novel deep unrolling architecture is proposed, whose key part is a dynamic proximal mapping module. Specifically, this module consists of a convolutional neural network (CNN) that learns/executes proximal mappings, and several multi-layer perception (MLP) blocks that perform dynamic modification mechanism to adjust the parameters of CNN given imaging conditions, which can be jointly trained end-to-end. In this way, MLP blocks will dynamically adjust the learned proximal operators at inference stage and make the unrolling network adapt to any given imaging setting.

The effectiveness of the proposed method is verified on three representative CSI applications, *i.e.*, image compressive sensing, CS-MRI, and CPR under various imaging conditions. Furthermore, the applicability of the proposed framework is explored on multiple CSI modalities with different imaging conditions. Experimental results demonstrate that the proposed method can not only effectively tackle varying imaging conditions for a specific CSI task, but also be able to handle multiple CSI modalities via only *one single model* simultaneously, and outperform the state-of-the-art approaches.

Our main contributions can be summarized as follows:

- We present the first dynamic proximal unrolling network (dubbed DPUNet) that can adaptively handle different imaging conditions, and even various CSI modalities via only one trained model.
- The key part of DPUNet is to develop a dynamic proximal mapping module, which can enable on-the-fly parameter’s adjustment at inference stage and boost the generalizability of deep unrolling networks.
- Experimental results demonstrate DPUNet can outper-

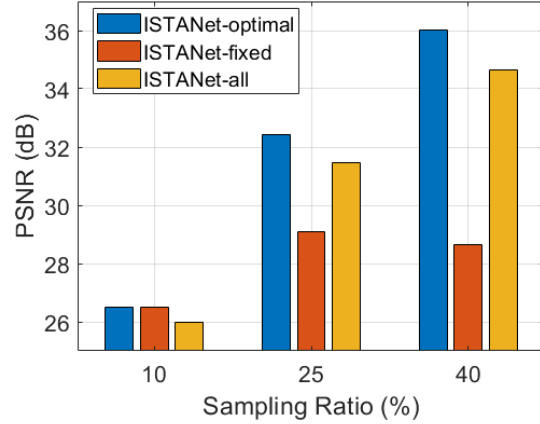


Fig. 2. The model generalizability test of a representative deep unrolling method – ISTANet [30] for image compressive sensing under multiple sampling ratios. “ISTANet-optimal” denotes the (three) models trained and tested on consistent sampling ratios. “ISTANet-fixed” indicates the single model trained on the fixed sampling ratio 10% and then tested on all sampling ratios. “ISTANet-all” implies the single model trained and tested on all sampling ratios (*i.e.*, 10%, 25% and 40%).

form the state-of-the-art on image compressive sensing, CS-MRI, and CPR under various imaging conditions without retraining. In addition, we show the extension of DPUNet can simultaneously handle all these CSI tasks via one single trained model, with promising results.

The remainder of this paper is organized as follows. We review related CSI methods in Section II. In Section III, the details of the proposed method including unrolling frameworks and dynamic proximal mapping module are presented. Section IV provides both experimental settings and qualitative results. In Section V, we conclude the paper.

II. RELATED WORK

Traditionally, the CSI problem can be attacked by variational optimization methods by minimizing the following cost functional:

$$\underset{x}{\text{minimize}} \quad \frac{1}{2} \|y - \Phi(x)\|_2^2 + \lambda \mathcal{R}(x), \quad (1)$$

by an iterative optimization framework, *e.g.*, the proximal gradient descent (PGD) [17], the alternating direction method of multipliers (ADMM) [21], iterative shrinkage-thresholding algorithm (ISTA) [19], and the half-quadratic splitting (HQS) [20] algorithm. In the above, $\mathcal{R}(x)$ indicates the regularization term associated with the prior knowledge of images, which alleviates the ill-posedness of CSI problems. Many image priors have been designed in imaging community over the past decades. The well-known examples include structured sparsity [12, 31, 32], group sparse representation (GSR) [15] and nonlocal low-rank [13, 14, 33].

In contrast to handcrafted priors, deep learning based CSI approaches have been proposed and demonstrated promising reconstruction results with fast inference speed [24–26, 34–36]. A stacked denoising auto-encode (SDA) was first applied to learn statistical dependencies from training data and improve signal recovery performance [24]. Fully-connected neural networks were proposed for image and video block-based

compressed sensing (BCS) reconstruction [25, 35]. Further several CNN-based CSI approaches were developed, which learn the inverse map from compressively sensed measurements to reconstructed images [26, 34, 36]. The basic idea of these works is designing a neural network $f_{NN}(y, \Theta)$ to directly perform the inverse mapping from observed measurements y to desired images x by learning network parameters Θ based upon the training dataset Γ :

$$\hat{\Theta} = \operatorname{argmin}_{\Theta} \frac{1}{|\Gamma|} \sum_{(y,x) \in \Gamma} \mathcal{L}(x, f_{NN}(y, \Theta)), \quad (2)$$

where \mathcal{L} is a loss function. However, these network architectures are predefined and fixed for specific problems and usually cannot adapt to others without retraining. In addition, designing neural networks could be often considered as much an art as a science, without clear theoretical guideline and domain knowledge [37].

Inspired by the interpretability and flexibility of traditional approaches, an emerging technique called deep unrolling or unfolding has been applied in CSI [27–30]. By unrolling the iterative optimization framework and introducing learnable parameters Θ , deep unrolling networks can be learned by minimizing the following empirical risk:

$$\hat{\Theta} = \operatorname{argmin}_{\Theta} \frac{1}{|\Gamma|} \sum_{(y,x) \in \Gamma} \mathcal{L}(x, f_{NN}(y, A, \Theta)), \quad (3)$$

where A is the given physical measurement model. Preliminary attempts focused on learning fast approximation of specialized iterative solvers attached to well-designed priors. The computation schemes of the resulting networks concise with the original solvers, but with fixed numbers of iterations and some untied/unshared parameters across layers/iterations. Well-known examples include learned shrinkage-thresholding algorithms (LISTA) [27] and learned approximate message passing (LAMP) algorithms [28]. Similar idea has also been applied on alternating direction method of multipliers (ADMM) solvers for CS-MRI [38], but with the goal to design powerful networks (ADMM-Net) rather than approximating variational methods. In contrast with encoding the sparsity on linear transform domain to network [38], ISTA-Net [30] goes beyond that to nonlinear transform domain sparsity. Moreover, these learned sparsity constraints can be further released into purely data-driven prior to boost the performance [39–43]. Nevertheless, few works consider the performance degradation of deep unrolling networks under mismatched imaging settings during inference, owing to the fixed learned network parameters. To the best of our knowledge, this paper is the first work that presents a novel dynamic deep unrolling network to solve this issue.

Another approach that can combine the benefits of both deep learning and optimization methods is called plug-and-play (PnP) priors [44]. Its core idea is to plug a denoiser into the iterative optimization such that the image prior is implicitly defined by the denoiser itself. Many deep learning-based denoisers have been utilized in the PnP framework to resolve CSI problems, without the need for task-specific training [45–50]. The main strength of PnP over deep unrolling

is the generalizability (only one network is required to handle various CSI problems [45]), but its performance often lags behind the deep unrolling due to the lack of end-to-end training [43]. Meanwhile, it also faces the limitations of high computational complexity and difficulties of tuning parameters [48]. In this work, we propose a dynamic proximal unrolling approach that improves the generalizability of deep unrolling considerably, while still enjoying the joint optimization of parameters via end-to-end learning.

III. METHOD

In this section, we first briefly introduce the iterative proximal optimization algorithms and the corresponding deep unrolling networks. What's more, we offer the insight into the design choices, including the choice of the optimization framework to unroll, and the CNN structure. Then, we describe the dynamic proximal mapping module – a core component of the proposed dynamic proximal unrolling network.

A. Proximal optimization and deep unrolling

A large variety of first-order proximal algorithms have been developed for solving Eq.(1) efficiently [17, 19–21]. In this paper, we adopt three representative proximal optimization frameworks (*i.e.*, PGD, HQS, and ADMM) to construct deep unrolling networks. It has been observed that all of them perform well with the proposed dynamic unrolling network structure. In the following, we discuss these design choices in detail and present final choice guided by empirical results.

Unrolled-PGD. In this paper, we adopt the proximal gradient descent method [17] for solving Eq.(1), whose iterations can be written as

$$z_k = x_{k-1} - r_{k-1} \nabla D(x_{k-1}), \quad (4)$$

$$x_k = \operatorname{Prox}_{\lambda \mathcal{R}}(z_k), \quad (5)$$

where k denotes the iteration index, the data-fidelity term $D(x) = \frac{1}{2} \|y - \Phi(x)\|_2^2$, ∇ denotes the vector differential operator that calculates the gradient of a given function, and r_k is step-size of the k -th iteration.

Eq.(4) can be understood as one-step gradient descent for dealing with the data-fidelity term. And $\operatorname{Prox}_{\lambda \mathcal{R}}(z) := \operatorname{argmin}_x \{\mathcal{R}(x) + \frac{1}{2\lambda} \|x - z\|_2^2\}$ denotes the proximal operator corresponding to the regularizer [18, 19] in Eq.(5). For instance, the proximal operator corresponds to soft-thresholding and shrinkage in a certain domain such as Wavelet, or Fourier, when there is a ℓ_1 -norm regularization for sparse coding [18, 51].

Given the modular nature of proximal optimization schemes, the whole iterations process can be truncated and unrolled into a trainable reconstruction network by replacing all instances of the proximal operator $\operatorname{Prox}_{\lambda \mathcal{R}}(\cdot)$ with a trainable deep convolutional neural network (CNN) mapping from images to images. The CNN is expected to learn to approximate the proximal mapping in Eq.(5). In this paper, we design a simple yet effective CNN consisting of five convolution (Conv) layers separated by an instance normalization (IN) layer [52] and a rectified linear unit (ReLU). IN was first proposed

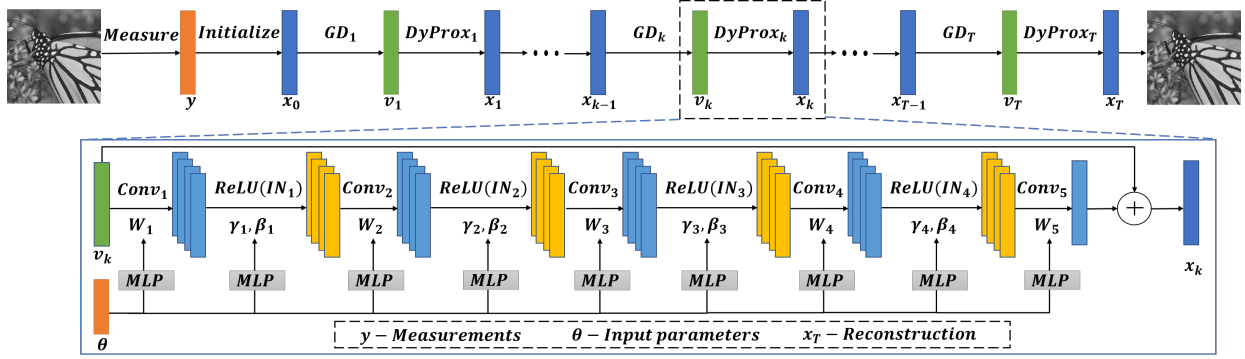


Fig. 3. Overview of the proposed dynamic proximal unrolling network. Specifically, our network is unrolled by T iterations (empirically set to 10), and each iteration includes the gradient descent (GD) and proposed dynamic proximal ($DyProx$) mapping module, which strictly corresponds to Eq. (4) and Eq. (5). The $DyProx$ consists of a deep convolutional neural network (CNN) and several multi-layer perception (MLP) blocks. The CNN is designed as a combination of five convolution (Conv) layers, each of which is separated by an instance normalization (IN) layer and a ReLU non-linearity. An identity skip connection is added between the input and output of the CNN. Mathematically, in the k -th iteration, the CNN maps z_k to x_k through

$$\begin{aligned} f_0 &= z_k, \\ f_j &= \text{ReLU}(\text{IN}_j(W_j * f_{j-1})), \quad j = 1, 2, 3, 4, \\ x_k &= W_5 * f_4 + f_0, \end{aligned}$$

where W_j represents the filters of convolution with a certain kernel and stride size, $*$ denotes the convolution operation, and the IN_j represents the j -th instance normalization operation as

$$\text{IN}_j(x) = \gamma_j \left(\frac{x - u(x)}{\sigma(x)} + \beta_j \right),$$

where γ_j and β_j are affine parameters learned from data; $u(x)$ and $\sigma(x)$ are the mean and standard deviation of the input x , computed across spatial dimensions independently for each feature channel and each sample.

Unrolled-HQS. HQS tackles Eq.(1) by introducing an auxiliary variable z , leading to iteratively solving subproblems for z and x as

$$z_k = \underset{z}{\operatorname{argmin}} \left\{ \frac{1}{2} \|y - \Phi(z)\|_2^2 + \frac{\mu_k}{2} \|z - x_{k-1}\|_2^2 \right\}, \quad (6)$$

$$x_k = \underset{x}{\operatorname{argmin}} \left\{ \lambda \mathcal{R}(x) + \frac{\mu_k}{2} \|z_k - x\|_2^2 \right\}, \quad (7)$$

where k denotes the iteration index, μ_k indicates the penalty parameter.

Assuming that $\Phi(\cdot)$ is a linear measurement model, we still adopt one-step gradient descent and proximal mapping to deal with Eq.(6) and Eq.(7), respectively, which can be written as

$$z_k = z_{k-1} - r_{k-1} (\Phi^T (\Phi z_{k-1} - y) + \mu_k (z_{k-1} - x_{k-1})), \quad (8)$$

$$x_k = \operatorname{Prox}_{\frac{\lambda}{\mu_k} \mathcal{R}} (z_k), \quad (9)$$

where Φ^T denotes the transpose of the sampling matrix, Prox denotes the proximal operator, and r_k is step-size at k -th iteration.

Once the proximal optimization is determined, the next step is to unroll the iterative process into a deep proximal unrolling network by introducing the designed CNN. In this way, the CNN and free hyper-parameters of optimization algorithms (*i.e.*, r_k , μ_k) can be jointly learned via end-to-end training.

Unrolled-ADMM. Eq.(1) can also be solved by ADMM, whose iterations can be written as

$$x_k = \operatorname{Prox}_{\lambda \mathcal{R}} (z_{k-1} - u_{k-1}), \quad (10)$$

$$z_k = \operatorname{Prox}_{\frac{1}{\mu_k} \mathcal{D}} (x_k + u_{k-1}), \quad (11)$$

$$u_k = u_{k-1} + x_k - z_k, \quad (12)$$

where $\mathcal{D}(x) = \frac{1}{2} \|y - \Phi(x)\|_2^2$, μ_k still indicates the penalty parameter.

Similarly, we use one-step gradient descent to tackle Eq.(11). Unrolled-ADMM can be derived by unrolling the corresponding iterative optimization and replacing the proximal operator with the designed convolutional neural network (CNN).

TABLE I
COMPARISONS OF UNROLLING NETWORKS BASED ON PGD, HQS, AND ADMM. WE SHOW PSNRs (DB) OF IMAGE CS RECONSTRUCTIONS UNDER VARIOUS SAMPLING RATIOS ON SET11.

| EXTENSIONS | SAMPLING RATIOS | | | |
|-------------|-----------------|-------|-------|-------|
| | 10% | 25% | 40% | 50% |
| PUNet-PGD | 26.57 | 31.80 | 34.85 | 36.12 |
| DPUNet-PGD | 27.31 | 32.99 | 36.48 | 38.35 |
| PUNet-HQS | 26.05 | 31.18 | 34.16 | 35.55 |
| DPUNet-HQS | 26.74 | 32.49 | 36.08 | 38.04 |
| PUNet-ADMM | 26.16 | 31.30 | 34.33 | 35.80 |
| DPUNet-ADMM | 26.80 | 32.51 | 36.05 | 38.02 |

Based on empirical results, we adopt the proximal gradient descent framework as the final choice, owing to its conciseness and effectiveness. More experimental details are presented in Section IV.

B. Dynamic proximal mapping module

Given the training data, the resulting networks can be trained end-to-end to learn the proximal mapping. However, the trainable parameters (*i.e.*, W_j, γ_j, β_j) of the CNN are usually fixed once trained, while different imaging conditions such as varying sampling-ratios or noise-levels all affect the performance of fixed proximal mapping.

To overcome this limitation, we make a step forward by proposing a dynamic proximal mapping module that can dynamically adjust the parameters of CNN according to different imaging conditions, to perform adaptively proximal mapping operators. To this end, we use several multi-layer perception (MLP) blocks, whose inputs are imaging parameters θ , such as the sampling ratio, and outputs are the parameters (W_j, γ_j, β_j) of CNN. The MLP blocks aim to generate and update the parameters of CNN, *i.e.*, the weights of convolution filters and affine parameters of IN layers. In the training stage, the proximal CNN and MLP blocks can be jointly trained. In the inference stage, given different imaging parameters, MLP blocks will adaptively adjust the parameters of the proximal CNN, thus improving the representation capability.

In the MLP blocks for convolution layers, the imaging parameter is an auxiliary input that feeds into fully-connected layers with the final layer outputting the convolution filter weights. The MLP output is reshaped into a 4D tensor of convolution filter weights, and convolved with the input image. Based empirical results in Section IV, we employ single fully-connected layer to directly learn the weights of convolution filters, which can be written as

$$W_j = \Phi_j \theta + b_j, \quad j = 1, \dots, 5, \quad (13)$$

where $\theta \in \mathbb{R}^l$ is the l input parameters related to the imaging settings, $W_j \in \mathbb{R}^{m_j}$ represents the weights (m_j denotes the total number of parameters) of the j -th convolution layer in CNN, and $\Phi_j \in \mathbb{R}^{m_j \times l}$, $b_j \in \mathbb{R}^{m_j}$ are the weight and bias of the corresponding fully-connected layer.

In essence, these fully-connected layers introduce a dynamic modulation mechanism for the weight of convolution with input parameters. Considering a special case, when the input parameters $\theta = 0$, it is mathematically equivalent to directly learning the weight of convolution without fully-connected layers, *i.e.*, $W_j = b_j, j = 1, \dots, 5$.

In the MLP blocks for IN layers, we employ two fully-connected layers separated by a ReLU (non-linearity) for the affine parameters of instance normalization in the CNN, respectively, which can be written as

$$Q_j = \Phi_{j2} \text{ReLU}(\Phi_{j1} \theta + b_{j1}) + b_{j2}, \quad j = 1, \dots, 4, \quad (14)$$

where $Q_j \in \mathbb{R}^m$ represents the parameters $\gamma_j \in \mathbb{R}^m$ or $\beta_j \in \mathbb{R}^m$ of the j -th instance normalization, $\Phi_{j1} \in \mathbb{R}^{m \times l}, \Phi_{j2} \in \mathbb{R}^{m \times m}, b_{j1} \in \mathbb{R}^m, b_{j2} \in \mathbb{R}^m$ are the weight and bias of the corresponding two fully-connected layers. Note that continually increasing the fully-connected layers can still improve the performance, but with more learnable parameters and computational complexity, provided in Section IV.

C. Dynamic proximal unrolling network

In essence, the structure of proposed dynamic proximal unrolling network (dubbed DPUNet) is derived from the truncated proximal gradient descent algorithm, combined with dynamic proximal mapping module. An overview of the proposed DPUNet is shown in Fig. 3.

When given training data, the inputs of the proposed DPUNet are the measurements y , corresponding physical forward model A and imaging parameters θ , which are sent to the reconstruction process and all MLP blocks, respectively. So the proposed DPUNet can be trained by minimizing the following empirical risk:

$$\hat{\Theta} = \underset{\Theta}{\operatorname{argmin}} \quad \frac{1}{|\Gamma|} \sum_{(y,x) \in \Gamma} \mathcal{L}(x, f_{NN}(y, A, g(\theta; \Theta))), \quad (15)$$

where $g(\cdot; \Theta)$ is the operation for generating the dynamic parameters via MLP blocks, and $\mathcal{L}(\cdot, \cdot)$ is exploited by the pixel-wise L_2 loss.

Given input parameters, MLP blocks will update the parameters of CNN to perform proximal mapping at each iteration. Finally, the outputs of proposed network are reconstructed images, which are used to compute loss with the ground-truth. By the back-propagation, the trainable parameters of our network, including the weight and bias of MLP blocks and the gradient step sizes, can be jointly optimized.

Once the model is trained, given the measurements and input parameters, the MLP blocks can adaptively generate parameters of CNN, and the unrolling network performs the reconstructions. In this way, we can dynamically adjust the parameter values of the CNN based on MLP blocks at the inference stage, thus enabling handling different imaging settings and continuous parameter control.

IV. EXPERIMENTS

In this section, we mainly focus on three representative CSI modalities: image compressive sensing, compressive sensing magnetic resonance imaging (CS-MRI), and compressive phase retrieval (CPR), and detail experiments to evaluate the proposed method. We first describe the experimental setting including both image formation models and implementation details. Then we conduct comprehensive ablation studies to investigate and analyze the performance of DPUNet. Moreover, we compare our method against prior art on different tasks under varying imaging conditions and provide an in-depth discussion of the proposed method. Finally, we present an extension of the proposed DPUNet to simultaneously handle all these CSI modalities via one single model.

A. Experimental Setting

1) *Image CS:* Image compressive sensing (CS) is a popular and well-studied linear CSI problem, which enables image or video capturing under a sub-Nyquist sampling rate [2, 54]. Following common practices in previous CS work, we focus on block-based compressive sensing (BCS) task to validate the proposed method. Given the sampling ratio, the measurement matrix Φ is a random Gaussian matrix and the measurement is

generated by $y = \Phi x$, where x is the vectorized version of an image block with size of 33×33 . For BCS, we adopt the data-fidelity term $D(x) = \frac{1}{2}||y - \Phi x||_2^2$, and compute its gradient $\nabla D(x) = \Phi^T(\Phi x - y)$. Here Φ^T denotes the transpose of Φ . For initialization, we adopt the linear mapping method, same as ISTA-Net [30]. For fair comparison, we utilize the same training data pairs in ISTA-Net [30] for training and widely used public dataset Set11 [55] for testing. In ablation study, we simulate to generate the BCS measurement of each patch with the sampling ratio η uniformly sampled from $[0.01, 0.04, 0.1, 0.25, 0.4, 0.5]$ under noise-free conditions. For further performance comparison, we add Gaussian noise with the noise level α uniformly sampled from $[0, 50]$ and take $[\eta, \alpha]$ as imaging parameters during training because there will always be noise in real CS measurements.

2) *CS-MRI*: CS-MRI is a mature technique for fast MRI through reconstruction of MR images from much fewer under-sampled measurements in k-space (*i.e.*, Fourier domain). Following the common practices, we adopt the measurement matrix with the form $\Phi = PF$, where F represents the 2-dimensional Fourier transform and P is an under-sampling matrix taken as commonly used pseudo radial sampling mask. We use the same training and testing brain medical images as ISTANet [30]. For initialization, we project the under-sampled Fourier measurements to image domain via the inverse Fourier transform. For each image, we simulate to generate subsampled measurements in Fourier domain with the sampling ratio η uniformly sampled from $[0.2, 0.3, 0.4, 0.5]$ and add Gaussian noise ϵ with the noise level α uniformly sampled from $[0, 50]$.

3) *CPR*: Compressive phase retrieval (CPR) is a representative non-linear inverse problem, concerned with the recovery of an underlying image from only the intensity of its complex transform. Mathematically, the measurements of CPR can be written as $y = |Ax|^2 + \epsilon$ with $\epsilon \sim \mathcal{N}(0, \alpha^2 \text{Diag}(|Ax|^2))$, where the term α controls the noise level in this problem [47, 56]. The data-fidelity term is the amplitude loss function $D(x) = \frac{1}{2}||\sqrt{y} - |Ax||_2^2$, whose surprising behavior was shown in [56]. Notice $D(x)$ involves complex number operations, we therefore adopt the Wirtinger derivatives [57] to compute its gradient, *i.e.*, $\nabla D(x) = A^H \left((|Ax| - \sqrt{y}) \circ \frac{Ax}{|Ax|} \right)$, where \circ denotes the Hadamard (element-wise) product and A^H denotes the conjugate transpose of A . We test CPR methods under simulated coded Fourier measurements, where the measurement matrix with the form $A = JFM$, where F represents the 2-dimensional Fourier transform, M is diagonal matrices with nonzero elements drawn uniformly from unit circle in the complex plane [47] and J is an $m \times n$ matrix made from randomly sampled rows of an $n \times n$ identity matrix. Here we initialize x_0 with a vector of ones worked sufficiently well. To train the network, we follow the common practice that uses 160000 overlapping patches (with size 64×64) cropped from 400 images from the BSD dataset [58]. For each patch, we simulate to generate coded Fourier measurements with the sampling ratio η uniformly sampled from $[0.3, 0.4, 0.5]$ and add Poisson shot noise ϵ with the noise level α uniformly sampled from $[0, 50]$.

The inputs of our network are the measurements and corre-

sponding normalized imaging parameters. We train all models using pixel-wise L_2 loss and Adam optimizer with PyTorch on one Nvidia GeForce GTX 2080 Ti GPU. The models of BCS are trained in 200 epochs with batch size 64 and learning rate 10^{-4} . The model of CS-MRI is trained in 200 epochs with batch size 4 and learning rate 10^{-4} . The model of CPR is trained in 20 epochs with batch size 20 and learning rate 10^{-3} .

B. Ablation Study

1) *Effects of different dynamic architectures*: To give some insights of the proposed dynamic proximal mapping module, we conduct an ablation study on different dynamic network architectures, including (1) PUNet: the basic proximal unrolling network without MLP blocks; (2) PUNet + DConv1: PUNet with dynamic convolution via one fully-connected layer; (3) PUNet + DConv2: PUNet with dynamic convolution via two fully-connected layers; (4) PUNet + DIn1: PUNet with dynamic instance normalization via one fully-connected layer; (5) PUNet + DIn2: PUNet with dynamic instance normalization via two fully-connected layers; (6) PUNet + DIn3: PUNet with dynamic instance normalization via three fully-connected layers; (7) PUNet + DConv1In1: PUNet with dynamic convolution and instance normalization via one fully-connected layer; (8) PUNet + DConv2In1: PUNet with dynamic convolution via two fully-connected layers and instance normalization via one fully-connected layer; (9) PUNet + DConv2In2: PUNet with dynamic convolution and instance normalization via two fully-connected layers; (10) DPUNet: PUNet with dynamic convolution via one fully-connected layer and dynamic instance normalization via two fully-connected layers. All models are trained and tested on image CS task with the same experimental setting.

To compare the performance, we show PSNRs (dB) of BCS reconstructions ($\eta = 10\%, 25\%, 40\%$) on Set11 with different structures and the number of model parameters (Million), provided in Table II. It can be seen that the performance of PUNet could be obviously improved by using dynamic convolution or dynamic instance normalization with two fully-connected layers, especially by using them together. Considered by the complexity of model, our final choice (*i.e.*, DPUNet) achieves performance near to the top with a reasonable number of parameters.

2) *Effects of different optimization frameworks*: To provide the insight into choice of optimization framework to unroll, we compare performance of the proposed three unrolling frameworks on image CS task, including their unrolled networks and corresponding dynamic versions. In Table I, it can be seen that the proposed dynamic proximal mapping module can consistently boost the performance of unrolling network derived from PGD, HQS, and ADMM, with average performance gain 1.45dB, 1.60dB, and 1.45dB, respectively. Meanwhile, DPUNet-PGD achieves the highest performance under various sampling ratios compared against other networks, chosen as the final choice.

TABLE II

COMPARISONS OF DIFFERENT STRUCTURES IN PROPOSED DYNAMIC PROXIMAL MAPPING MODULE. WE SHOW PSNRs (dB) OF BCS RECONSTRUCTIONS UNDER MULTIPLE CS RATIOS ON SET11 WITH DIFFERENT ARCHITECTURES AND THE NUMBER OF MODEL PARAMETERS (MILLION). THE BEST RESULTS ARE LABELED IN **BOLD** AND THE SECOND BEST RESULTS ARE UNDERLINED.

| ARCHITECTURES | CS RATIOS | | | PARAMS |
|-------------------|--------------|--------------|--------------|--------|
| | 10% | 25% | 40% | |
| PUNet | 26.57 | 31.80 | 34.85 | 1.12 |
| PUNet + DConv1 | <u>26.87</u> | 32.47 | 35.50 | 2.24 |
| PUNet + DConv2 | 27.05 | 32.73 | 36.05 | 72.65 |
| PUNet + DIn1 | 26.87 | 32.39 | 35.70 | 1.13 |
| PUNet + DIn2 | 27.15 | 32.74 | 36.12 | 1.46 |
| PUNet + DIn3 | 27.25 | 32.85 | 36.23 | 1.79 |
| PUNet + DConv1In1 | 26.49 | 32.04 | 34.84 | 2.25 |
| PUNet + DConv2In1 | 26.76 | 32.51 | 35.92 | 72.66 |
| PUNet + DConv2In2 | 27.33 | 32.99 | <u>36.42</u> | 72.98 |
| DPUNet | <u>27.31</u> | <u>32.99</u> | 36.48 | 2.58 |

C. Performance Comparison

1) *Validations on BCS*: To verify the performance of the proposed method, we mainly compare it against three classic CS approaches, namely TVAL3 [59], D-AMP [16], NLR-CS [13], the learning-based approach ReconNet [26] and the representative deep unrolling approach ISTA-Net [30]. Recent works (*e.g.*, SCSNet [36] and OPINE-Net [60]) use data-driven learned sampling matrix to achieve very high performance ¹. For fair comparison, in this paper, we only consider the competing methods using fixed sampling matrix. We use the code made available by the respective authors on their websites. For end-to-end training methods, such as ReconNet and ISTA-Net, we train the corresponding model for each sampling ratio setting. Table III shows all methods performance on the Set11 public dataset under various sampling ratios and noise levels. It can be observed that our method outperforms other methods under various sampling ratios via one single trained model. By contrast with ISTA-Net and ReconNet, our method avoids the cumbersome retraining requirement, which is beneficial for real application. In addition, it is worth mentioning that our method can generalize well to the unseen case during training setting, as $\eta = 30\%$. We show the reconstructions of all algorithms under imaging conditions $\eta = 10\%$, $\alpha = 10$, in Fig. 4. It can be seen that DPUNet produces more accurate and clearer reconstructed images than other competing algorithms.

2) *Validations on CS-MRI*: We mainly compare DPUNet with five competing approaches for CS-MRI, including three classic algorithms RecPF [22], FCSA [61] and D-MRI [62], the plug-and-play (PnP) approach IRCNN [49]², and the deep unrolling network ISTANet [30]. We train separate models

¹Despite these gains induced by data-driven sampling matrix, the existing SOTA methods still suffer from the lack of generalization and universality. For example, OPINE-Net is designed for each sampling ratio owing to predefined CNN filters of Sampling Subnet and requires separately trained. SCSNet is specifically designed for BCS task, and not trivial to adapt to other CS imaging modalities, *e.g.*, CS-MRI.

²Note that the state-of-the-art PnP approach TFPnP [48] can only handle the fixed size (*i.e.*, 128×128 pixels) of MR images owing to the introduction of a fully-connected layer internally, and not adapt to our testing dataset.

of ISTANet for each sampling ratio setting in 200 epochs. Table IV shows the quantitative performance comparisons on 50 brain medical images under different imaging conditions. It can be seen that DPUNet significantly outperforms other competing algorithms under various imaging conditions with only one trained model. The fact that one single DPUNet model performed so well on all sampling ratios, particularly in comparison to the ISTA-Net models, which were trained separately per sampling ratio, again demonstrates that DPUNet generalizes across measurement matrices. What's more, compared with the plug-and-play approach IRCNN, deep unrolling networks ISTA-Net and DPUNet both enjoy higher reconstruction performance and faster run time owing to end-to-end training. In Fig. 5, we show the reconstructions of three brain MR images and corresponding PSNRs under different sampling ratios ($\eta = 20\%, 30\%, 40\%$) and noise levels ($\alpha = 10, 30, 50$) with six algorithms. It can be observed that DPUNet can reconstruct more details and sharper edges, especially in case of severe noise.

3) *Validations on CPR*: We mainly compare DPUNet with two state-of-the-art approaches (BM3D-prGAMP [50] and prDeep [47]) for CPR. We use their respective authors' implementations and adopt the twelve images used in [47] to quantitatively evaluate different CPR methods. The results of performance comparisons for CPR are summarized in Table V. It can be seen that DPUNet can handle these imaging settings with state-of-the-art results via one single trained network. The visual comparison can be found in Fig. 6. It can be found that our method can still effectively recover desired images, and produce clearer results than other competing methods.

D. Discussion

1) *Generalizability of DPUNet*: In order to further investigate the generalizability of DPUNet, we train and test DPUNet on consistent CS ratios, denoted by DPUNet-optimal. Fig. 7 shows the comparison between the "DPUNet-optimal", "DPUNet", and "PUNet" model for image compressive sensing under multiple CS ratios. Note that "DPUNet-optimal" denotes the (three) models of DPUNet separately trained and tested on each CS ratio, which are expected to get the optimal results. "DPUNet" and "PUNet" indicate the single model trained and tested on all CS ratios, and the main difference of them is that "DPUNet" adopts the proposed dynamic module which "PUNet" lacks.

It can be observed that single trained model of DPUNet can achieve very close performance (the average PSNR difference is about 0.24 dB) with the optimal results, while there is a large gap (the average PSNR difference is about 2.18 dB) between "PUNet" model and the optimal model. Overall, we demonstrate that proposed dynamic proximal mapping module can obviously boost the generalizability of deep unrolling network, avoiding time-consuming and storage-consuming retraining.

2) *Robustness on input parameters mismatch*: In practical applications, while the sampling ratio can be accurately measured, the noise level or signal-to-noise ratio (SNR) is often estimated by related methods [63–65] since the ground truth is unknown. So it is necessary for DPUNet to be robust to

TABLE III

AVERAGE PSNR (dB) PERFORMANCE COMPARISONS FOR BCS RECONSTRUCTIONS ON SET11 UNDER DIFFERENT IMAGING CONDITIONS (η AND α DENOTE THE SAMPLING RATIO AND NOISE LEVEL RESPECTIVELY). THE BEST RESULTS ARE LABELED IN **BOLD** AND THE SECOND ARE UNDERLINED.

| SAMPLING RATIO | NOISE LEVEL | TVAL3 | D-AMP | NLR-CS | ReconNet | ISTA-Net | ISTA-Net ⁺ | DPUNet |
|----------------|---------------|-------|-------|--------|----------|--------------|-----------------------|--------------|
| $\eta = 50\%$ | $\alpha = 10$ | 26.83 | 30.63 | 26.12 | 25.60 | 30.74 | <u>31.42</u> | 31.99 |
| | $\alpha = 30$ | 19.08 | 25.92 | 19.84 | 24.39 | 26.36 | <u>26.87</u> | 27.20 |
| | $\alpha = 50$ | 14.88 | 23.56 | 15.62 | 22.34 | 23.85 | <u>24.30</u> | 24.79 |
| $\eta = 40\%$ | $\alpha = 10$ | 26.31 | 29.29 | 25.16 | 25.19 | 28.73 | <u>30.53</u> | 31.20 |
| | $\alpha = 30$ | 19.33 | 25.08 | 20.05 | 23.78 | 25.42 | <u>26.21</u> | 26.59 |
| | $\alpha = 50$ | 15.38 | 22.84 | 16.08 | 21.56 | 23.14 | <u>23.78</u> | 24.17 |
| $\eta = 30\%$ | $\alpha = 10$ | 25.57 | 27.58 | 24.42 | 24.23 | 27.07 | <u>29.45</u> | 30.04 |
| | $\alpha = 30$ | 19.47 | 23.93 | 20.51 | 23.12 | 24.46 | <u>25.28</u> | 25.70 |
| | $\alpha = 50$ | 15.81 | 22.00 | 16.70 | 21.24 | 22.30 | <u>22.89</u> | 23.29 |
| $\eta = 10\%$ | $\alpha = 10$ | 21.91 | 20.87 | 21.48 | 21.91 | 23.33 | <u>24.63</u> | 25.40 |
| | $\alpha = 30$ | 18.83 | 19.68 | 20.23 | 20.92 | 21.30 | <u>21.85</u> | 22.26 |
| | $\alpha = 50$ | 16.34 | 18.53 | 17.83 | 19.19 | 19.47 | <u>20.02</u> | 20.32 |
| $\eta = 1\%$ | $\alpha = 10$ | 11.26 | 5.20 | 11.43 | 17.04 | 17.17 | <u>17.25</u> | 17.27 |
| | $\alpha = 30$ | 10.90 | 5.19 | 10.93 | 16.44 | <u>16.47</u> | 16.46 | 16.58 |
| | $\alpha = 50$ | 10.55 | 5.18 | 10.51 | 15.45 | <u>15.45</u> | 15.44 | 15.79 |

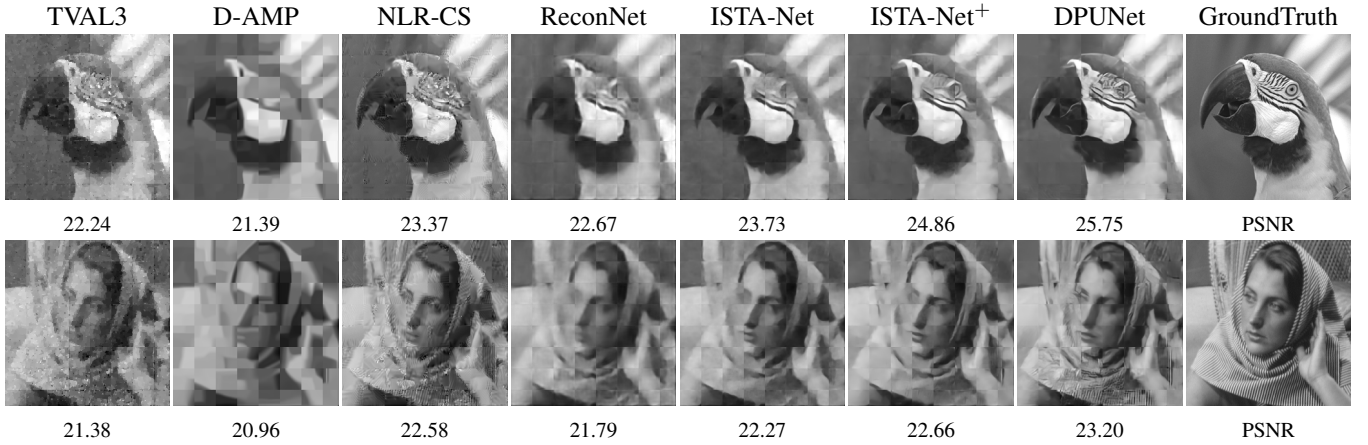


Fig. 4. Reconstructed images and corresponding PSNRs from CS measurements under imaging conditions ($\eta = 10\%$, $\alpha = 10\%$) with seven CS algorithms.

TABLE IV

AVERAGE PSNR (dB) AND RUN TIME (s) PERFORMANCE COMPARISONS FOR CS-MRI ON 50 BRAIN MEDICAL IMAGES UNDER DIFFERENT IMAGING CONDITIONS (η AND α DENOTE THE SAMPLING RATIO AND NOISE LEVEL RESPECTIVELY). THE BEST RESULTS ARE LABELED IN **BOLD** AND THE SECOND BEST RESULTS ARE UNDERLINED.

| ALGORITHM | $\eta = 20\%$ | | | $\eta = 30\%$ | | | $\eta = 40\%$ | | | $\eta = 50\%$ | | | TIME CPU/GPU |
|-----------|---------------|--------------|--------------|---------------|--------------|--------------|---------------|--------------|--------------|---------------|--------------|--------------|-----------------|
| | $\alpha = 10$ | 30 | 50 | |
| RecPF | 31.41 | 25.06 | 21.33 | 32.47 | 24.76 | 20.61 | 33.05 | 24.37 | 19.96 | 33.46 | 24.00 | 19.41 | 0.39s/- |
| FCSA | 30.71 | 24.11 | 19.19 | 31.31 | 23.07 | 17.93 | 31.28 | 22.28 | 17.21 | 31.29 | 21.78 | 16.77 | 0.64s/- |
| DMRI | 25.77 | 20.23 | 22.06 | 32.15 | 24.66 | 20.69 | 31.80 | 23.71 | 19.64 | 31.35 | 22.92 | 18.80 | 10.28s/- |
| IRCNN | 33.77 | 30.58 | 29.09 | 34.64 | 31.34 | 29.70 | 35.18 | 31.75 | 30.02 | 35.58 | 32.02 | 30.18 | -12.16s |
| ISTANet | 32.50 | <u>30.78</u> | <u>29.22</u> | 34.84 | <u>31.72</u> | <u>29.85</u> | <u>35.37</u> | <u>32.04</u> | <u>30.10</u> | <u>35.87</u> | <u>32.25</u> | <u>30.22</u> | -0.03s |
| DPUNet | 34.39 | 31.44 | 29.74 | 35.41 | 32.11 | 30.32 | 35.98 | 32.43 | 30.59 | 36.33 | 32.59 | 30.70 | -0.05s |

mismatched input parameters, mainly under noisy conditions. To analyze the robustness of DPUNet for the input parameters, we use a range of parameter values of the noise-level as the input at inference stage, and show average reconstruction results (PSNRs) on Set11 test set from noisy BCS measurements (sampling ratio $\eta = 30\%$, noise level $\alpha = 30$) as the input parameter changes. Fig. 8 illuminates that DPUNet is robust to the inaccuracy of input parameters – reaching similar reconstruction results under a range of input parameter mismatch. The visual comparisons can see Fig. 9, which also show visually similar results of reconstructed images.

3) *Hyper-parameters analysis*: We conduct a hyper-parameters analysis and train different models of our method, then present experimental results. Specifically, we focus on two hyper-parameters of our DPUNet, *i.e.*, unrolling iterations and training epochs. First, we unroll different numbers of proximal optimization iterations and train corresponding models. The performance of different models on image compressive sensing tasks are presented in Table VI. It can be seen that unrolling ten iterations is sufficient for our DPUNet to get promising results. Furthermore, We provide the performance of trained models on different epochs on image compressive

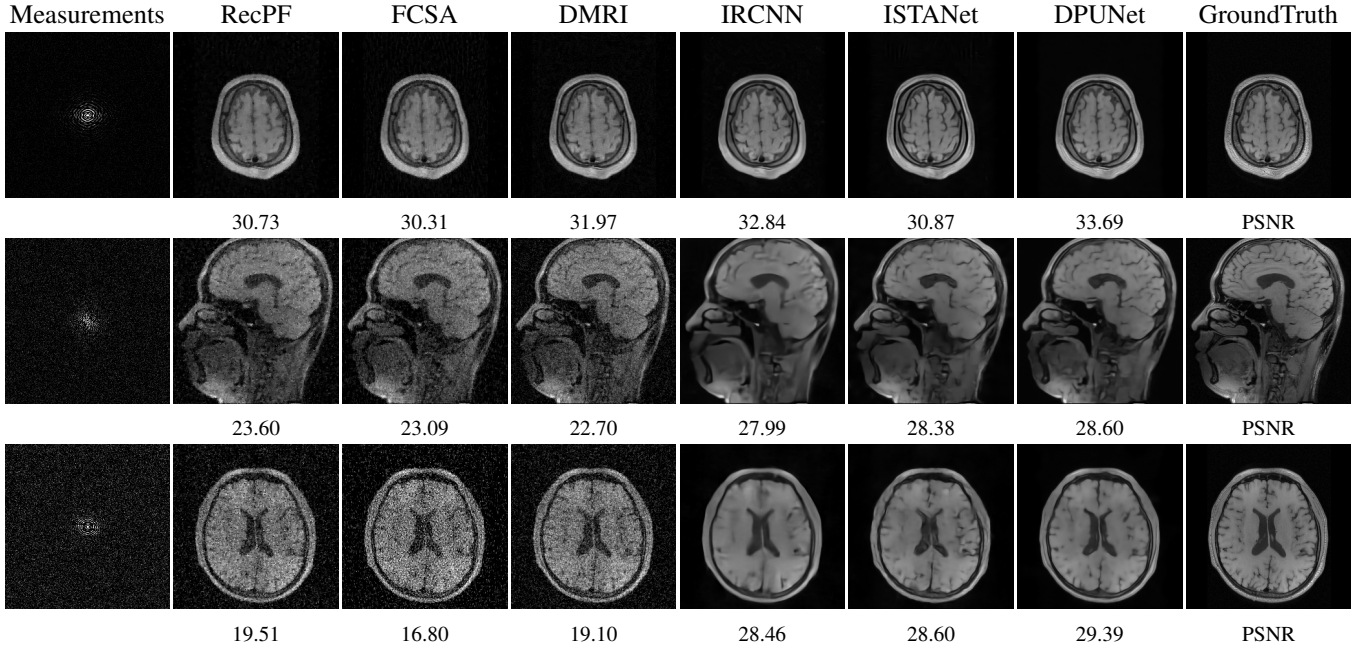


Fig. 5. Reconstructed images and corresponding PSNRs for CS-MRI under different sampling ratios ($\eta = 20\%, 30\%, 40\%$, from top to bottom) and different noise levels ($\alpha = 10, 30, 50$, from top to bottom) with six algorithms.

TABLE V

AVERAGE PSNR (dB) PERFORMANCE COMPARISONS FOR CPR ON TWELVE IMAGES UNDER DIFFERENT IMAGING CONDITIONS (η AND α DENOTE THE SAMPLING RATIO AND NOISE LEVEL RESPECTIVELY). THE BEST RESULTS ARE LABELED IN **BOLD** AND THE SECOND BEST RESULTS ARE UNDERLINED.

| η | α | prGAMP | prDeep | DPUNet |
|--------|----------|--------------|--------------|--------------|
| 50% | 10 | <u>31.56</u> | 30.64 | 33.14 |
| | 30 | 27.46 | <u>27.69</u> | 28.63 |
| 40% | 10 | <u>31.26</u> | 30.10 | 32.32 |
| | 30 | 26.77 | <u>27.46</u> | 28.31 |
| 30% | 10 | 29.05 | <u>30.00</u> | 30.96 |
| | 30 | 26.47 | <u>26.99</u> | 27.75 |

TABLE VI

AVERAGE PSNR (dB) PERFORMANCE COMPARISONS OF DPUNET WITH DIFFERENT UNROLLING ITERATIONS. THE BEST RESULTS ARE LABELED IN **BOLD** AND THE SECOND BEST RESULTS ARE UNDERLINED.

| MODEL | CS RATIO (ON SET11) | | | | |
|-----------|---------------------|--------------|--------------|--------------|--------------|
| | 4% | 10% | 25% | 40% | 50% |
| DPUNet-5 | 21.56 | 26.09 | 31.08 | 35.00 | 36.88 |
| DPUNet-10 | <u>22.09</u> | <u>27.04</u> | <u>32.73</u> | <u>36.22</u> | <u>38.07</u> |
| DPUNet-15 | 22.14 | 27.08 | 32.76 | 36.23 | 38.13 |

sensing task in Fig. 10. It can be observed that our model trained by 200 epochs can achieve satisfactory performance.

E. Extension for multiple CSI tasks

Inspired by the same network structure of solving CSI problems, we explore the potential of our method to handle multiple imaging modalities with one single trained model simultaneously. To verify this claim, we present an extension of our method and run a mixed experiment, where

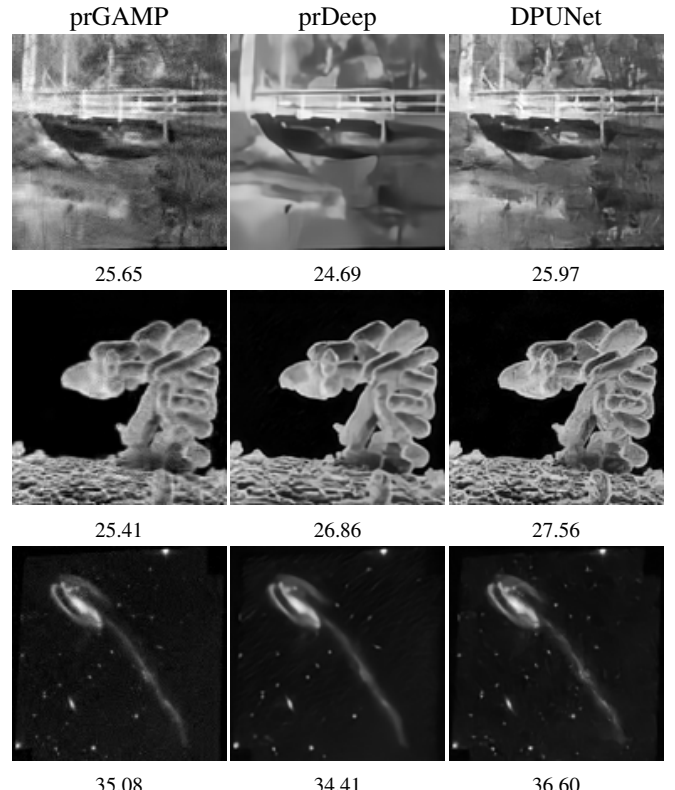


Fig. 6. Reconstructed images and corresponding PSNRs for CPR under different sampling ratios ($\eta = 30\%, 40\%, 50\%$, from top to bottom) and noise level ($\alpha = 10$) with three algorithms.

we consider three CSI modalities mentioned above under different sampling ratios with varying noise levels. In order to implement this, we simulate to generate the BCS measurements with the sampling ratio η uniformly sampled

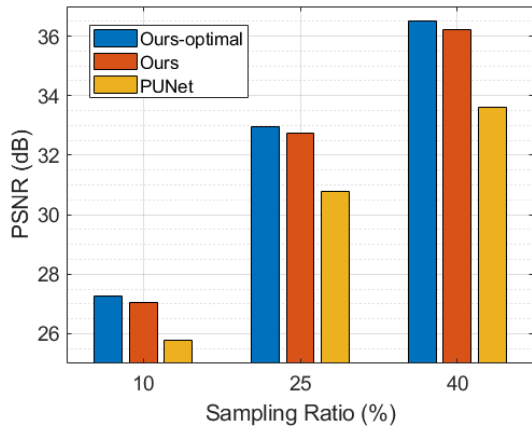


Fig. 7. The model generalizability test of our method for image compressive sensing under multiple sampling ratios. "Ours-optimal" denotes the (three) models trained and tested on consistent sampling ratios. "Ours" is the single model trained and tested on all sampling ratios. "PUNet" is the degraded version of "Ours" without dynamic module, and still the single model trained and tested on all sampling ratios.

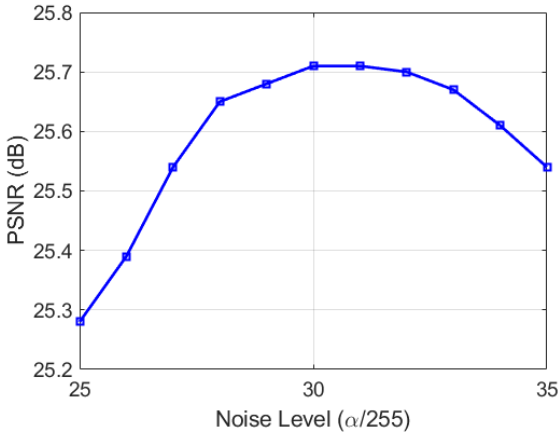


Fig. 8. The model robustness test of DPUNet with mismatched input parameters on noisy BCS measurements. The real imaging conditions are sampling ratio $\eta = 30\%$, noise level $\alpha = 30$. Here we test DPUNet under a range of parameter values of the noise level as the input, and show corresponding reconstruction results (PSNR) on Set11 as the input parameter α changes.

from [0.01, 0.04, 0.1, 0.25, 0.4, 0.5] from CS training data-set, CS-MRI measurements with the sampling ratio η uniformly sampled from [0.2, 0.3, 0.4, 0.5] from MRI training data-set, and the under-sampling coded diffraction measurements uniformly sampled from [0.3, 0.4, 0.5] from CPR training data-set, all adding noise levels α uniformly sampled from [0, 50].

Moreover, we increase an input parameter κ to represent the imaging modality³, and the other parameter is related to the imaging condition (η, α) . During training, the BCS, CS-MRI and CPR training data pairs that include image patches and corresponding measurements are alternately fed to our network, together with imaging parameters. The network is trained in 200000 iterations with using pixel-wise L_2 loss and

³For simplicity, we input the parameters $\kappa = 1$ for dealing with BCS task, $\kappa = 2$ for CS-MRI, and $\kappa = 3$ for CPR.

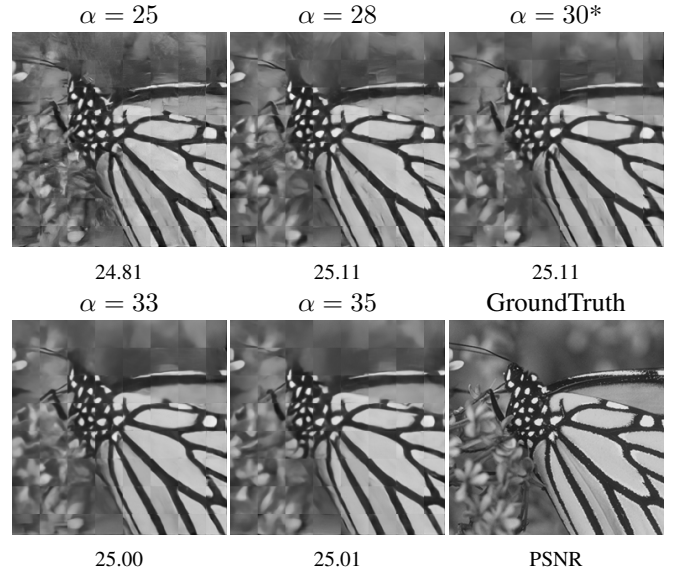


Fig. 9. Reconstructed images and corresponding PSNRs from noisy BCS measurements ($\eta = 30\%$, $\alpha = 30$) under a range of parameter values of the noise-level at inference stage.

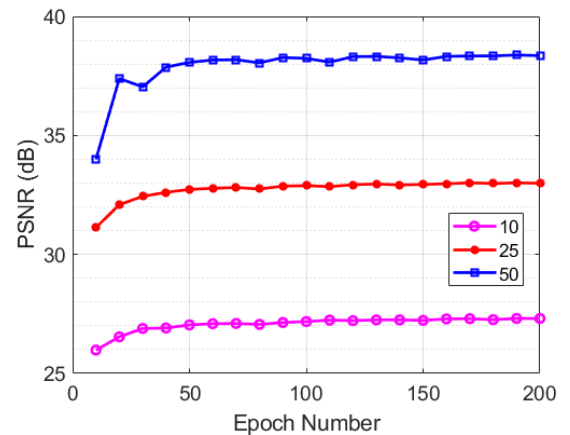


Fig. 10. The model performance of BCS reconstructions ($\eta = 10\%, 25\%, 50\%$) on Set11 under different training epochs.

Adam optimizer with learning rate 10^{-4} . It takes about 18 hours to train the model.

The reconstruction results with the extension of our method for all imaging modalities and imaging conditions are provided in Table VII. We can see that our method can not only handle various imaging conditions, but also totally different imaging modalities via one single model without retraining. Here we also compare with the results of our baselines, which represent the models of DPUNet trained on single imaging task (BCS, CS-MRI, or CPR), respectively. It can be seen that the extension of our method still achieves close results to the baselines, despite small performance degradation. It means with the same network structure, our method is able to handle different CSI tasks via one single trained model without losing much accuracy. We show reconstructed results of single trained model for multiple CSI modalities with noise level ($\alpha = 10$) and different sampling ratios ($\eta = 10\%$ for BCS, $\eta = 20\%$ for CS-MRI, $\eta = 50\%$ for CPR) in Fig. 1. It can be found that

the proposed network is flexible for various imaging conditions and universal for different CSI modalities.

TABLE VII

RECONSTRUCTION RESULTS WITH OUR SINGLE TRAINED MODEL (OURS*) FOR DIFFERENT IMAGING MODALITIES UNDER VARYING IMAGING CONDITIONS. THE BASELINES ARE THE MODELS OF DPUNET SEPARATELY TRAINED ON SINGLE IMAGING TASK (BCS, CS-MRI AND CPR), WHICH REPRESENT THE PERFORMANCE STANDARD.

| Task | η | α | Ours* | Baselines |
|--------|--------|----------|-------|-----------|
| BCS | 30% | 10 | 29.96 | 30.04 |
| | | 30 | 25.57 | 25.70 |
| | 50% | 10 | 31.89 | 31.99 |
| | | 30 | 27.03 | 27.20 |
| CS-MRI | 30% | 10 | 35.08 | 35.41 |
| | | 30 | 31.61 | 32.08 |
| | 50% | 10 | 35.97 | 36.33 |
| | | 30 | 32.07 | 32.59 |
| CPR | 30% | 10 | 30.56 | 30.96 |
| | | 30 | 27.75 | 27.75 |
| | 50% | 10 | 32.91 | 33.14 |
| | | 30 | 28.38 | 28.63 |

V. CONCLUSION

We have proposed a dynamic proximal unrolling network for a variety of compressive imaging problems under varying imaging conditions. The main contribution of the proposed method is developing a dynamic proximal mapping module, which can dynamically update parameters of the proximal network at inference stage and make it adapt to any given imaging setting and even imaging task. As a result, the proposed method is able to handle a wide range of compressive imaging modalities, including image compressive sensing, CS-MRI, and compressive phase retrieval under varying imaging conditions via one single trained model. Experimental results demonstrate the effectiveness and state-of-the-art performance of the proposed method. Thereby, we envision the proposed network to be applied into embedded mobile devices where storage and computational resources demands become prohibitive, and to handle a variety of imaging tasks via only one trained model.

REFERENCES

- [1] D. L. Donoho, “Compressed sensing,” *IEEE Transactions on information theory*, vol. 52, no. 4, pp. 1289–1306, 2006.
- [2] A. Liutkus, D. Martina, S. Popoff, G. Chardon, O. Katz, G. Lerose, S. Gigan, L. Daudet, and I. Carron, “Imaging with nature: Compressive imaging using a multiply scattering medium,” *Scientific reports*, vol. 4, p. 5552, 2014.
- [3] M. F. Duarte, M. A. Davenport, D. Takhar, J. N. Laska, T. Sun, K. F. Kelly, and R. G. Baraniuk, “Single-pixel imaging via compressive sampling,” *IEEE signal processing magazine*, vol. 25, no. 2, pp. 83–91, 2008.
- [4] R. Kerviche, N. Zhu, and A. Ashok, “Information-optimal scalable compressive imaging system,” in *Computational Optical Sensing and Imaging*. Optical Society of America, 2014, pp. CM2D-2.
- [5] A. C. Sankaranarayanan, C. Studer, and R. G. Baraniuk, “Cs-muvi: Video compressive sensing for spatial-multiplexing cameras,” in *2012 IEEE International Conference on Computational Photography (ICCP)*. IEEE, 2012, pp. 1–10.
- [6] M. Lustig, D. Donoho, and J. M. Pauly, “Sparse mri: The application of compressed sensing for rapid mr imaging,” *Magnetic Resonance in Medicine: An Official Journal of the International Society for Magnetic Resonance in Medicine*, vol. 58, no. 6, pp. 1182–1195, 2007.
- [7] M. Lustig, D. L. Donoho, J. M. Santos, and J. M. Pauly, “Compressed sensing mri,” *IEEE signal processing magazine*, vol. 25, no. 2, pp. 72–82, 2008.
- [8] F. Rousset, N. Ducros, A. Farina, G. Valentini, C. D’Andrea, and F. Peyrin, “Adaptive basis scan by wavelet prediction for single-pixel imaging,” *IEEE Transactions on Computational Imaging*, vol. 3, no. 1, pp. 36–46, 2016.
- [9] M. L. Moravec, J. K. Romberg, and R. G. Baraniuk, “Compressive phase retrieval,” in *Wavelets XII*, vol. 6701. International Society for Optics and Photonics, 2007, p. 670120.
- [10] H. Ohlsson, A. Yang, R. Dong, and S. Sastry, “Cprl—an extension of compressive sensing to the phase retrieval problem,” *Advances in Neural Information Processing Systems*, vol. 25, pp. 1367–1375, 2012.
- [11] S. Ma, W. Yin, Y. Zhang, and A. Chakraborty, “An efficient algorithm for compressed mr imaging using total variation and wavelets,” in *IEEE Conference on Computer Vision and Pattern Recognition (CVPR)*. IEEE, 2008, pp. 1–8.
- [12] H. Y. Liao and G. Sapiro, “Sparse representations for limited data tomography,” in *IEEE International Symposium on Biomedical Imaging: From Nano to Macro*. IEEE, 2008, pp. 1375–1378.
- [13] W. Dong, G. Shi, X. Li, Y. Ma, and F. Huang, “Compressive sensing via nonlocal low-rank regularization,” *IEEE Transactions on Image Processing*, vol. 23, no. 8, pp. 3618–3632, 2014.
- [14] X. Qu, Y. Hou, F. Lam, D. Guo, J. Zhong, and Z. Chen, “Magnetic resonance image reconstruction from undersampled measurements using a patch-based nonlocal operator,” *Medical Image Analysis*, vol. 18, no. 6, pp. 843–856, 2014.
- [15] J. Zhang, D. Zhao, and W. Gao, “Group-based sparse representation for image restoration,” *IEEE Transactions on Image Processing*, vol. 23, no. 8, pp. 3336–3351, 2014.
- [16] C. A. Metzler, A. Maleki, and R. G. Baraniuk, “From denoising to compressed sensing,” *IEEE Transactions on Information Theory*, vol. 62, no. 9, pp. 5117–5144, 2016.
- [17] P. L. Combettes and J.-C. Pesquet, “Proximal splitting methods in signal processing,” in *Fixed-point algorithms for inverse problems in science and engineering*. Springer, 2011, pp. 185–212.
- [18] M. V. Afonso, J. M. Bioucas-Dias, and M. A. Figueiredo, “Fast image recovery using variable splitting and constrained optimization,” *IEEE transactions on image processing*, vol. 19, no. 9, pp. 2345–2356, 2010.
- [19] A. Beck and M. Teboulle, “A fast iterative shrinkage-thresholding algorithm for linear inverse problems,” *SIAM Journal on Imaging Sciences*, vol. 2, no. 1, pp. 183–202, 2009.
- [20] D. Geman and C. Yang, “Nonlinear image recovery with half-quadratic regularization,” *IEEE transactions on Image Processing*, vol. 4, no. 7, pp. 932–946, 1995.
- [21] S. Boyd, N. Parikh, E. Chu, B. Peleato, J. Eckstein, et al., “Distributed optimization and statistical learning via the alternating direction method of multipliers,” *Foundations and Trends® in Machine learning*, vol. 3, no. 1, pp. 1–122, 2011.
- [22] J. Yang, Y. Zhang, and W. Yin, “A fast alternating direction method for tvl1-l2 signal reconstruction from partial fourier data,” *IEEE Journal of Selected Topics in Signal Processing*, vol. 4, no. 2, pp. 288–297, 2010.
- [23] G. Ongie, A. Jalal, C. A. Metzler, R. G. Baraniuk, A. G. Dimakis, and R. Willett, “Deep learning techniques for inverse problems in imaging,” *IEEE Journal on Selected Areas in Information Theory*, vol. 1, no. 1, pp. 39–56, 2020.
- [24] A. Mousavi, A. B. Patel, and R. G. Baraniuk, “A deep learning approach to structured signal recovery,” in *2015 53rd annual allerton conference on communication, control, and computing (Allerton)*. IEEE, 2015, pp. 1336–1343.
- [25] M. Iliadis, L. Spinoulas, and A. K. Katsaggelos, “Deep fully-connected networks for video compressive sensing,” *Digital Signal Processing*, vol. 72, pp. 9–18, 2018.
- [26] K. Kulkarni, S. Lohit, P. Turaga, R. Kerviche, and A. Ashok, “Reconnet: Non-iterative reconstruction of images from compressively sensed measurements,” in *Proceedings of the IEEE Conference on Computer Vision and Pattern Recognition*, 2016, pp. 449–458.
- [27] K. Gregor and Y. LeCun, “Learning fast approximations of sparse coding,” in *Proceedings of the 27th international conference on international conference on machine learning*, 2010, pp. 399–406.
- [28] M. Borgerding, P. Schniter, and S. Rangan, “Amp-inspired deep networks for sparse linear inverse problems,” *IEEE Transactions on Signal Processing*, vol. 65, no. 16, pp. 4293–4308, 2017.

[29] Y. Yang, J. Sun, H. Li, and Z. Xu, "Deep admm-net for compressive sensing mri," in *Proceedings of the 30th international conference on neural information processing systems*, 2016, pp. 10–18.

[30] J. Zhang and B. Ghanem, "Ista-net: Interpretable optimization-inspired deep network for image compressive sensing," in *Proceedings of the IEEE conference on computer vision and pattern recognition*, 2018, pp. 1828–1837.

[31] S. Mun and J. E. Fowler, "Block compressed sensing of images using directional transforms," in *2009 16th IEEE international conference on image processing (ICIP)*. IEEE, 2009, pp. 3021–3024.

[32] S. Ravishankar and Y. Bresler, "Mr image reconstruction from highly undersampled k-space data by dictionary learning," *IEEE Transactions on Medical Imaging*, vol. 30, no. 5, pp. 1028–1041, 2010.

[33] J. Mairal, F. R. Bach, J. Ponce, G. Sapiro, and A. Zisserman, "Non-local sparse models for image restoration," in *The IEEE International Conference on Computer Vision (ICCV)*, vol. 29, 2009, pp. 54–62.

[34] A. Mousavi and R. G. Baraniuk, "Learning to invert: Signal recovery via deep convolutional networks," in *IEEE International Conference on Acoustics, Speech and Signal Processing (ICASSP)*. IEEE, 2017, pp. 2272–2276.

[35] A. Adler, D. Boulil, M. Elad, and M. Zibulevsky, "A deep learning approach to block-based compressed sensing of images," *arXiv preprint arXiv:1606.01519*, 2016.

[36] W. Shi, F. Jiang, S. Liu, and D. Zhao, "Scalable convolutional neural network for image compressed sensing," in *Proceedings of the IEEE/CVF Conference on Computer Vision and Pattern Recognition*, 2019, pp. 12 290–12 299.

[37] J. R. Hershey, J. L. Roux, and F. Weninger, "Deep unfolding: Model-based inspiration of novel deep architectures," *arXiv preprint arXiv:1409.2574*, 2014.

[38] J. Sun, H. Li, Z. Xu, et al., "Deep admm-net for compressive sensing mri," in *Advances in neural information processing systems*, 2016, pp. 10–18.

[39] C. Metzler, A. Mousavi, and R. Baraniuk, "Learned d-amp: Principled neural network based compressive image recovery," in *Advances in Neural Information Processing Systems*, 2017, pp. 1772–1783.

[40] H. K. Aggarwal, M. P. Mani, and M. Jacob, "Modl: Model-based deep learning architecture for inverse problems," *IEEE transactions on medical imaging*, vol. 38, no. 2, pp. 394–405, 2018.

[41] W. Dong, P. Wang, W. Yin, G. Shi, F. Wu, and X. Lu, "Denoising prior driven deep neural network for image restoration," *IEEE Transactions on Pattern Analysis and Machine Intelligence*, vol. 41, no. 10, pp. 2305–2318, 2018.

[42] L. Wang, C. Sun, Y. Fu, M. H. Kim, and H. Huang, "Hyperspectral image reconstruction using a deep spatial-spectral prior," in *Proceedings of the IEEE/CVF Conference on Computer Vision and Pattern Recognition*, 2019, pp. 8032–8041.

[43] K. Zhang, L. V. Gool, and R. Timofte, "Deep unfolding network for image super-resolution," in *Proceedings of the IEEE/CVF Conference on Computer Vision and Pattern Recognition*, 2020, pp. 3217–3226.

[44] S. V. Venkatakrishnan, C. A. Bouman, and B. Wohlberg, "Plug-and-play priors for model based reconstruction," in *IEEE Global Conference on Signal and Information Processing*. IEEE, 2013, pp. 945–948.

[45] J. Rick Chang, C.-L. Li, B. Poczos, B. Vijaya Kumar, and A. C. Sankaranarayanan, "One network to solve them all—solving linear inverse problems using deep projection models," in *Proceedings of the IEEE International Conference on Computer Vision*, 2017, pp. 5888–5897.

[46] T. Meinhardt, M. Moller, C. Hazirbas, and D. Cremers, "Learning proximal operators: Using denoising networks for regularizing inverse imaging problems," in *Proceedings of the IEEE International Conference on Computer Vision*, 2017, pp. 1781–1790.

[47] C. A. Metzler, P. Schniter, A. Veeraraghavan, and R. G. Baraniuk, "prdeep: Robust phase retrieval with a flexible deep network," in *international conference on machine learning*, 2018, pp. 3498–3507.

[48] K. Wei, A. Aviles-Rivero, J. Liang, Y. Fu, C.-B. Schönlieb, and H. Huang, "Tuning-free plug-and-play proximal algorithm for inverse imaging problems," in *International Conference on Machine Learning*. PMLR, 2020, pp. 10 158–10 169.

[49] K. Zhang, W. Zuo, S. Gu, and L. Zhang, "Learning deep cnn denoiser prior for image restoration," in *Proceedings of the IEEE conference on computer vision and pattern recognition*, 2017, pp. 3929–3938.

[50] M. Mardani, Q. Sun, D. Donoho, V. Palyan, H. Monajemi, S. Vasanawala, and J. Pauly, "Neural proximal gradient descent for compressive imaging," in *Advances in Neural Information Processing Systems*, 2018, pp. 9573–9583.

[51] D. Ulyanov, A. Vedaldi, and V. Lempitsky, "Improved texture networks: Maximizing quality and diversity in feed-forward stylization and texture synthesis," in *Proceedings of the IEEE Conference on Computer Vision and Pattern Recognition*, 2017, pp. 6924–6932.

[52] K. He, X. Zhang, S. Ren, and J. Sun, "Identity mappings in deep residual networks," in *European conference on computer vision*. Springer, 2016, pp. 630–645.

[53] A. C. Sankaranarayanan, L. Xu, C. Studer, Y. Li, K. F. Kelly, and R. G. Baraniuk, "Video compressive sensing for spatial multiplexing cameras using motion-flow models," *SIAM Journal on Imaging Sciences*, vol. 8, no. 3, pp. 1489–1518, 2015.

[54] B. M. Roth S., "Fields of experts," in *IEEE Conference on Computer Vision and Pattern Recognition*, 2009, p. 205.

[55] L. Yeh, J. Dong, J. Zhong, L. Tian, M. Chen, G. Tang, M. Soltanolkotabi, and L. Waller, "Experimental robustness of fourier ptychography phase retrieval algorithms," *Optics Express*, vol. 23, no. 26, pp. 33 214–33 240, 2015.

[56] E. J. Candes, X. Li, and M. Soltanolkotabi, "Phase retrieval via wirtinger flow: Theory and algorithms," *IEEE Transactions on Information Theory*, vol. 61, no. 4, pp. 1985–2007, 2015.

[57] D. Martin, C. Fowlkes, D. Tal, and J. Malik, "A database of human segmented natural images and its application to evaluating segmentation algorithms and measuring ecological statistics," in *Proceedings Eighth IEEE International Conference on Computer Vision. ICCV 2001*, vol. 2. IEEE, 2001, pp. 416–423.

[58] C. Li, W. Yin, H. Jiang, and Y. Zhang, "An efficient augmented lagrangian method with applications to total variation minimization," *Computational Optimization and Applications*, vol. 56, no. 3, pp. 507–530, 2013.

[59] J. Zhang, C. Zhao, and W. Gao, "Optimization-inspired compact deep compressive sensing," *IEEE Journal of Selected Topics in Signal Processing*, vol. 14, no. 4, pp. 765–774, 2020.

[60] J. Huang, S. Zhang, and D. Metaxas, "Efficient mr image reconstruction for compressed mr imaging," *Medical Image Analysis*, vol. 15, no. 5, pp. 670–679, 2011.

[61] E. M. Eksioglu, "Decoupled algorithm for mri reconstruction using nonlocal block matching model: Bm3d-mri," *Journal of Mathematical Imaging and Vision*, vol. 56, no. 3, pp. 430–440, 2016.

[62] D. R. Pauluzzi and N. C. Beaulieu, "A comparison of snr estimation techniques for the awgn channel," *IEEE Transactions on communications*, vol. 48, no. 10, pp. 1681–1691, 2000.

[63] M. Riffé, M. Blaimer, K. Barkauskas, J. Duerk, and M. Griswold, "Snr estimation in fast dynamic imaging using bootstrapped statistics," in *Proc Intl Soc Mag Reson Med*, vol. 1879, 2007.

[64] O. Dietrich, J. G. Raya, S. B. Reeder, M. F. Reiser, and S. O. Schoenberg, "Measurement of signal-to-noise ratios in mr images: influence of multichannel coils, parallel imaging, and reconstruction filters," *Journal of Magnetic Resonance Imaging: An Official Journal of the International Society for Magnetic Resonance in Medicine*, vol. 26, no. 2, pp. 375–385, 2007.